Slow-Light-Enhanced Optical Imaging of Microfiber Radius Variations with Subangstrom Precision

Michael Scheucher,[1] Khaled Kassem,[1] Arno Rauschenbeutel,[1,2] Philipp Schneeweiss,[1,2] and Jürgen Volz[1,2,*]

[1] *Atominstitut, TU Wien, Stadionallee 2, 1020 Vienna, Austria*
[2] *Department of Physics, Humboldt-Universität zu Berlin, 10099 Berlin, Germany*

(Received 27 July 2020; revised 16 October 2020; accepted 9 November 2020; published 16 December 2020)

Optical fibers play a key role in many different fields of science and technology. In particular, fibers with a diameter of several micrometers are intensively used in photonics. For these applications, it is often important to precisely know and control the fiber radius. Here we describe a technique to determine the radius profile of an optical microstructure with ultrahigh precision from a single optical image. Using a basic microscopy setup, we demonstrate our method by measuring the axial radius variation along a 30-μm-diameter silica fiber with precision less than 0.3 Å. The axial resolution is tens of micrometers, and the measurement range is more than 0.5 mm. Our method relies on imaging the fiber's whispering-gallery modes in which the speed of light propagating along the fiber axis is strongly reduced. Imaging those whispering-gallery modes, we infer the local radius variations of the optical microstructure with ultrahigh precision. Because of the performance and simplicity of implementation, we are convinced that our scheme has high potential for precision metrology and optical sensing.

DOI: 10.1103/PhysRevApplied.14.064052

I. INTRODUCTION

The resolution of optical far-field imaging systems is typically limited by diffraction. As a consequence, it is not possible to resolve details with a spacing smaller than half the wavelength of the imaging light. Even for high-end objectives with a numerical aperture of approximately 1, this limits the resolution to a few hundred nanometers when visible light is used. At the same time, the position of pointlike scatterers or emitters can be determined with almost arbitrary precision by fitting the point-spread function of the imaging system to the image [1]. This technique is used, for example, in superresolution microscopy [2] or quantum technology [3] and yields a position accuracy of a few nanometers. Other superresolution techniques rely on the spatially selective deactivation of fluorophores and are thus restricted to use in combination with certain emitters [2]. Despite these advances, the observation of subwavelength structures and size variations of macroscopic and microscopic objects is still challenging in many settings.

For example, most fabrication processes for optical fibers do not allow one to directly monitor the local fiber radius. Nevertheless, its precise knowledge is important for many applications. Scanning electron microscopy is a standard method to determine the size of objects with a resolution on the nanometer scale. However, this technique requires insertion of the fibers into a vacuum recipient, which limits the cycle time for analyzing fibers. Several methods that use fiber-guided light to determine the fiber radius have been demonstrated [4–9]. However, none of these schemes provide simultaneously good axial and nanometer-scale radial precision. Scanning methods that rely on spectroscopy using external probes, via, for example, a second fiber, enable good axial and radial resolution [10,11]. However, these approaches fall short of providing means to characterize many samples in a short time as the probe fiber has to be mechanically moved along the sample. Furthermore, for those approaches, the probe and the sample fiber are in direct mechanical contact, which potentially damages the sample when the two fibers are sliding over each other or when the fibers are being separated again. Other approaches, including measuring the force-elongation curve [12] or optical imaging methods [13,14], do not achieve sufficient precision.

Here we demonstrate a method that uses slow light to determine the radius profile of a sample microfiber with subangstrom precision while providing high axial resolution. Slow light has attracted much interest in recent years [15], resulting in various applications. For example, slow light emerging in photonic crystals has been used to realize sensors [16–18], amplifiers [19], enhancement of optical power densities [20–22], nonlinear optics [23,24], and optical delay lines [25].

---

[*] juergen.volz@hu-berlin.de

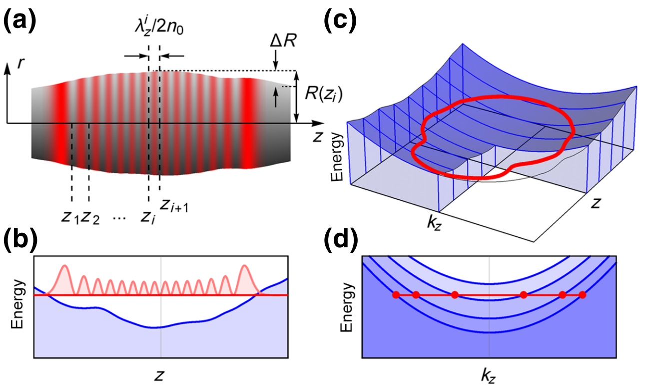

FIG. 1. (a) Side view of a fiber with nanoscale radius variation along the fiber axis (the radius variations are strongly exaggerated for illustration purposes). Because of these variations, a characteristic mode structure forms with clear intensity maxima and minima. The distance between two adjacent intensity minima is given by the axial wavelength $\lambda_z^i/2n_0$. For the sample fiber considered here, the central radius is a few tens of micrometers and the radius variation ΔR is on the order of a few nanometers. (b) The radius profile can be translated into a potential energy $V(z)$, which can support optical bound states (i.e. localized WGMs), indicated in red. (d) Axial dispersion relation of the photon energy $\hbar\omega(k_z)$ for different fiber radii. (c) Phase-space representation of a WGM with energy $\hbar\omega$ that is trapped in the potential formed by nanoscale radius variations along z. The red line indicates the phase-space trajectory of a classical particle trapped in the potential. Projecting the plot onto the z and k_z axes yields the cases shown in (b),(d), respectively.

We use slow light arising in the presence of whispering-gallery modes (WGMs), which naturally form around optical fibers [25]. WGMs are optical resonances in which light travels along the circumference of the fiber, undergoing continuous total internal reflection [26]. Because of the mostly azimuthal light propagation, the effective group velocity of light in the axial direction along the fiber is significantly reduced. In this situation, already small radius variations significantly alter the axial structure of the WGMs [see Fig. 1(a)]. At the same time, the slow group velocity in the axial direction results in a small axial wave vector. When the light forms a standing wave, this gives rise to intensity modulations of comparably large spatial period of the wave function. By imaging the light tunneling from these axial standing-wave WGMs into free-space using a CCD camera, we measure the axial-mode profile, from which we can precisely determine the radius profile of an optical fiber over a long segment of the fiber in single-shot operation.

II. THEORETICAL MODEL

When light circulates around the circumference of a fiber, the electric field $\mathbf{E}$ has to fulfill the Helmholtz equation:

$$[\nabla^2 + k^2 n^2(r)]\mathbf{E} = 0, \tag{1}$$

where $k = 2\pi/\lambda$ is the light's wave number and $n(r)$ describes the refractive index inside ($n = n_0$) and outside ($n \approx 1$) the fiber. When the radius variations of the fiber are sufficiently small, we can separate the propagation of the light into propagation parallel and propagation perpendicular to the fiber axis with respective wave vectors $\mathbf{k}_z$ and $\mathbf{k}_{\phi,r}$, where $\mathbf{k} = \mathbf{k}_z + \mathbf{k}_{\phi,r}$. This allows us to separate the Helmholtz equation using the ansatz $\mathbf{E} = \mathbf{\Phi}(\phi, r)\mathcal{Z}(z)$. For a given radius $R(z)$, the radial and azimuthal equations can be solved locally, yielding the resonance condition $k_{\phi,r}(z) = f(m,p)m/R(z)n_0$, where m and p are the azimuthal and radial quantum numbers of the WGM, respectively, and $f(m,p) \sim 1$ is a factor that describes the geometrical dispersion of the fiber [27]. The axial part can be described by the axial wave equation

$$\left(\partial_z^2 + k^2 n_0^2 - f^2 \frac{m^2}{R(z)^2}\right)\mathcal{Z}(z) = 0, \tag{2}$$

where we make use of $k^2 = k_z^2 + k_{\phi,r}^2$. Equation (2) is formally identical to a one-dimensional Schrödinger equation [5] and describes the propagation of a photon with effective mass $m_{\text{eff}} = \hbar k n_0^2/2c$ in the potential landscape that is set by the radius profile $R(z)$ with the potential $V(z)/(\hbar^2/2m_{\text{eff}}) = (mf)^2/R(z)^2$ [see Figs. 1(b) and 1(c)], where c is the vacuum speed of light. The local group velocity c_{gr} of light traveling along this potential can be obtained from the dispersion relation $\omega(k_z) = c/n_0\sqrt{k_{\phi,r}^2 + k_z^2}$ [see Fig. 1(d)] and is approximated to be $c_{\text{gr}} = d\omega/dk_z \approx c/n_0 \times k_z/k$ [25]. For light fields close to the band edge $k \approx k_\phi$, one obtains a very strong reduction in the group velocity (i.e., $c_{\text{gr}} \ll c$). Because of this group-velocity reduction, the phase velocity of the light in the axial direction $c_{\text{ph}} = c^2/n_0^2 c_{\text{gr}}$ is strongly increased. As the axial wavelength, λ_z, is directly proportional to c_{ph}, λ_z is significantly larger than the vacuum wavelength. Because of this magnification effect, the axial wavelength can now be measured with high accuracy, which in turn allows one to perform a high-accuracy measurement of the corresponding fiber radius variations. The dependency of the fiber radius on the local group velocity and thus on λ_z can be expressed as

$$R(z) = f(m,p)\frac{m\lambda}{2\pi\ n_0}\left[1 - \mathcal{S}(z)^2\right]^{-1/2}, \tag{3}$$

where we introduce the velocity reduction $\mathcal{S} = c_{\text{gr}}/c = \lambda/\lambda_z$. In our experiment, the axial radius variations that define the potential $V(z)$ result in bound states in the axial direction. For this case, the light oscillates between the two

TABLE I. Axial quantum number q, resonance wavelength λ_{vac}, mean axial wavelength $\overline{\lambda_z}/n_0$, mean group velocity reduction $\bar{S}$, and resulting mean enhancement factor $\overline{M}$ of the WGMs under examination.

q	λ_{vac} (nm)	$\overline{\lambda_z}/n_0$ (μm)	$\overline{S}$	$\overline{M}/10^3$
8	846.4819	68.8	0.0058	190
10	846.4724	63.5	0.0063	149
14	846.4569	55.8	0.0072	101
27	846.4007	40.9	0.0098	40
38	846.3500	34.4	0.0117	24

axial turning points, called the "caustics," creating a standing wave along the fiber, while still propagating along the circumference as a running wave. The number of nodes of the standing wave is labeled with the quantum number q. Measuring the intensity distribution of the axial standing wave allows one to determine the local axial wavelength λ_z [see Fig. 1(a)] and thus the local fiber radius with enhanced precision.

The radius variation can be determined, at best, with precision

$$\Delta R = \frac{\Delta\lambda_z}{M}, \tag{4}$$

where

$$M = \left|\frac{\partial\lambda_z}{\partial R(z)}\right| \approx \frac{2\pi}{mf}\frac{1}{\mathcal{S}^3} \tag{5}$$

is the enhancement factor and $\Delta\lambda_z$ is the error in determining λ_z, which is given by the optical resolution of the imaging system. For typical experimental parameters, $M = 10^4$–10^5 can easily be achieved; see Table I. From Eq. (4), it follows that the enhancement factor and thus the possible precision strongly increase with decreasing $\mathcal{S}$ (increasing λ_z). The increased precision of the measurement of the radius variation given in Eq. (4) is inherently connected with a decrease in axial resolution, which is given approximately by $\lambda_z/2n_0$. This can be seen as a direct consequence of the uncertainty principle, which prevents one from measuring both the position and the momentum with arbitrary precision.

III. SETUP AND MEASUREMENT PROCEDURE

In the following, the fiber under examination is referred to as the "sample fiber." To couple light into the sample fiber, we use a tapered fiber coupler. This coupling fiber is mounted on a translation stage and aligned perpendicular to the sample fiber. This allows us to evanescently couple light from the coupling fiber into the sample fiber; see Fig. 2(a). The coupling rate between the fibers can be adjusted via their relative distance. When light is sent through the coupling fiber and its frequency is scanned, WGMs are excited whenever the resonance condition is fulfilled and when the WGM has a finite mode overlap with the evanescent field of the coupling fiber. The excited WGMs can be observed with a CCD camera that images the mode structure along the sample fiber, as shown in Fig. 2(b). We emphasize that the collected light is not scattered from the surface but originates from tunneling of WGMs through the potential barrier imposed by the refractive-index jump at the fiber surface [28]. Hence, the imaging of the mode structure does not rely on local surface pollution or roughness but occurs for any structure supporting WGMs. For imaging, we use a CCD camera (mvBlueFox3, Matrix Vision) in combination with a standard microscope objective (Mitutoyo 10X M Plan APO LWD) with a numerical aperture of 0.28. The camera system and the coupling fiber are mounted on opposite sides of the sample fiber [see Fig. 2(a)]. This ensures a clear view of the WGMs with the camera. For the excitation of the WGMs, we use a tunable diode laser (Velocity Laser 6316, New Focus) with a wavelength of about 845 nm. To infer the radius profile from the camera images such as shown in Fig. 2(b), we use the following procedure (see also Ref. [27]). We determine the axial intensity profile of the WGM by averaging the axial intensity over several horizontal pixel lines. Then the positions of zero intensity z_i are extracted from a parabolic fit to the data points in the

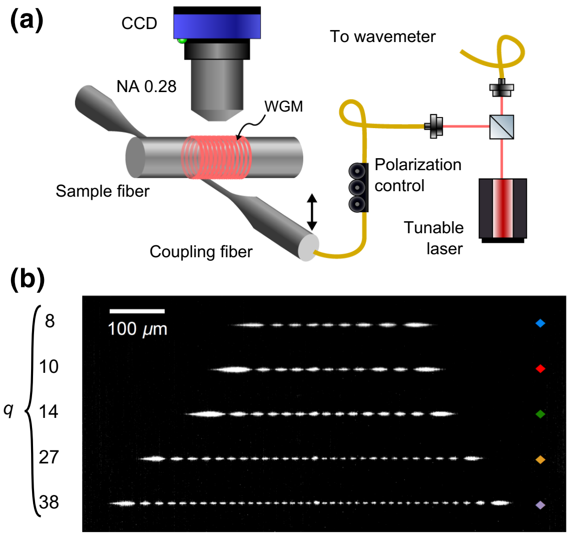

FIG. 2. (a) The experimental setup used to determine the radius profile of the sample fiber consists of a tunable diode laser, polarization controllers, a coupling fiber, and a CCD camera with an objective with a numerical aperture (NA) of 0.28. For further diagnostics, an additional photodiode can be used to monitor the fiber transmission, and the incident light is sent to a wavelength meter. (b) Micrographs of light tunneling out of the WGMs in the direction of the camera for different axial modes, $q \in \{8, 10, 14, 27, 38\}$, which are used for determining the local fiber radius in Fig. 3.

vicinity of the intensity minima. For our imaging system, this procedure enables us to determine these positions with a precision of $\Delta\lambda_z = 0.2\ \mu$m. To obtain the absolute value of the local radius, according to Eq. (3), we also require the azimuthal and radial quantum numbers, m and p, of the imaged WGM. Therefore, we compare the measured azimuthal free spectral range of different mode families with the free spectral range obtained from our numerically solving the radial wave equation of a dielectric cylinder.

IV. RESULTS AND PRECISION

For a sample fiber of approximately 30-μm diameter, we record two sets of images with the CCD camera. First, the coupling fiber is placed approximately at the center of the sample-fiber waist, and we perform five independent measurements of the radius profile by exciting five TE-polarized modes with different axial quantum number q but the same quantum numbers m and p. Figure 2(b) shows micrographs of the light tunneling out of the fiber for these WGMs. The resonance wavelengths, measured with a wavelength meter (High Finesse WS7-60), and the corresponding q values are summarized in Table I. The azimuthal and radial quantum numbers are determined to be $m = 117$ and $p = 8$, which corresponds to a factor $f(8, 117) = 1.426\,058\,43(1)$. The radius profiles of the fiber extracted from these images are shown in Fig. 3. The radius profiles obtained with different modes are in very good agreement with each other, illustrating the reproducibility of the method. It also becomes evident that with increasing axial resolution (for higher q), the radial resolution decreases, as expected for this measurement [see Eq. (4)]. To check if the position of the coupling fiber alters the measured radius profile, the measurement is repeated after the coupling fiber is moved by approximately 110 μm in the axial direction. The results are shown in Fig. 3(b) and are in very good agreement with the measurements in Fig. 3(a). In the measurements with the highest axial resolution (i.e., with the highest values of q), one observes a small distortion at the position of the coupling fiber. However, the errors introduced by scattered light from the coupling fiber are well below 1 nm and can be corrected by performing two measurements with different fiber positions. The radius obtained is an azimuthal average and thus the measurement does not provide information about the ellipticity of the fiber cross section.

Two different types of errors occur when one measures the radius profiles $R(z)$. On the one hand, there is a systematic error in the absolute radius $R_q = fm\lambda_q/n_0$, which amounts to an uncertainty of around ±1 nm in our case. This error is identical for each measurement and originates from the systematic error in determining λ, f, and n_0 in Eq. (3). For our setup, this is dominated by the limited knowledge of the refractive index of the sample fiber, n_0. On the other hand, the radius variations along the fiber, $R(z) - R_q$, can be measured with much higher accuracy and are, in our measurement, limited by the measurement accuracy of the axial wavelength λ_z [27].

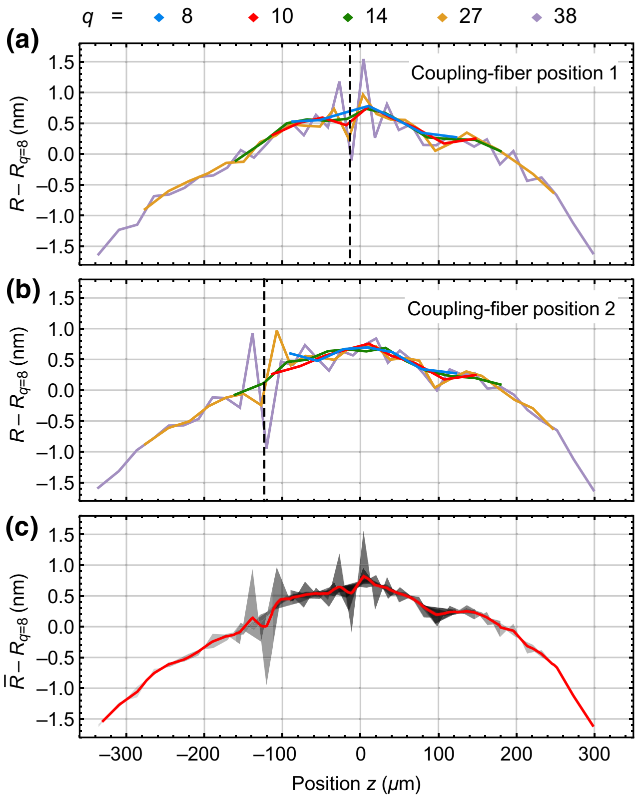

FIG. 3. (a) Evaluated radius profiles as a function of the position along the sample fiber for WGMs with different axial quantum numbers q. The position of the coupling fiber is indicated by the dashed vertical line. (b) Same as (a) only with the coupling fiber moved by approximately 110 μm. (c) Mean radius profile obtained when all measurements are taken into account (red line). The shaded area indicates the deviation of the individual measurements from the mean profile. For better visibility, we subtract the (constant) caustic radius of the sample fiber for the $q = 8$ mode, $R_{q=8} = 15.475(1)\ \mu$m.

From a total of ten individual measurements, we determine the most-likely fiber radius profile $\bar{R}$ by linearly interpolating the measurement points for each mode and taking the average over all modes. The resulting profile is shown in Fig. 3(c). It indicates an almost-perfect cylinder that has a residual radius variation of 2 nm over an axial extent of 600 μm.

To get an estimate of the precision of the individual measurements, we compute the deviation between each measurement point from the most-likely radius profile, $R - \bar{R}$, and plot a histogram of the deviations for each axial mode; see Fig. 4(a). The standard deviation of this difference $\sigma(R - \bar{R})$ gives an estimate of the error of our measurement of the radius variation along the fiber. Figure 4(b) shows this standard deviation as a function of

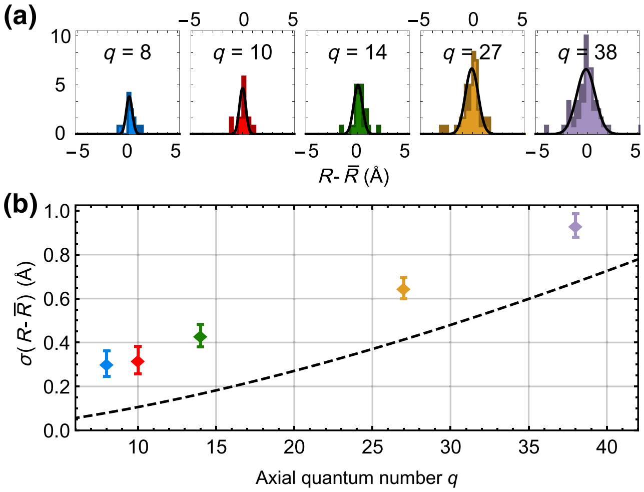

FIG. 4. (a) Histogram of the deviation for each individual measurement from the average radius profile $\overline{R}$ for different values of q. (b) Standard deviation of $R - \overline{R}$, obtained from the Gaussian fits in (a), as a function of q. The error bars show the standard errors for the parameter estimates of the fit. The dashed line corresponds to the theoretically expected mean standard error calculated by assuming a parabolic radius profile, which increases with increasing q.

q and a theoretical prediction for comparison (dashed line). To calculate the theoretical curve, we approximate the radius profile by a parabolic profile, from which we then estimate the average axial wavelength. Taking into account all known experimental errors, we derive the expected mean standard deviation of the axial radius profile [27]. Our analysis shows that the measurement precision of the radius variation increases with decreasing q, as expected. For all modes, we observe subangstrom precision, and for $q = 8$ we reach a precision of 0.30 ± 0.06 Å. Our precision inferred from the measurement data shows the same trend with q as the theoretical prediction.

V. SUMMARY AND OUTLOOK

In summary, we present a method that uses slow light to determine the radius variations along an optical fiber with subangstrom precision. Our approach offers significant practical benefits in comparison with scanning-probe techniques. For example, it provides radius information along the whole measurement range in a single shot, enabling fast data acquisition, and it is a noncontact scheme, thus, minimizing the risk of damaging the sample. As we discuss in Ref. [27], our method can also be performed with even-lower-cost equipment (i.e. without the optical wavelength meter), while still yielding subangstrom precision in the measurements.

Importantly, our results apply to any fiber or in general any optical system of any size that still supports WGMs, as long as a partial standing wave is formed along the fiber that can be resolved within the dynamic range of the camera (see the discussion in Ref. [27]). Even for radius profiles with no bound states, such a standing wave can be formed by launching the light from a point of a larger-fiber diameter [5]. Given the high achievable precision in conjunction with the simplicity of its implementation, we are convinced that our method is promising for technical applications such as *in situ* monitoring of fiber and microfiber fabrication and that it has high potential for precision metrology and optical sensing [29].

ACKNOWLEDGMENTS

The authors are grateful to T. Hoinkes for technical support. This work received funding from the European Commission under the projects ErBeStA (Grant No. 800942) and NanoQuaNt, the Austrian Academy of Sciences (ÖAW; ESQ Discovery Grant QuantSurf), and the Austrian Science Fund under the project NanoFiRe (Grant No. P 31115).

M.S. and K.K. contributed equally to this work.

[1] R. E. Thompson, D. R. Larson, and W. W. Webb, Precise nanometer localization analysis for individual fluorescent probes, Biophys. J. **82**, 2775 (2002).

[2] S. W. Hell, Far-field optical nanoscopy, Science **316**, 1153 (2007).

[3] J. D. Wong-Campos, K. G. Johnson, B. Neyenhuis, J. Mizrahi, and C. Monroe, High-resolution adaptive imaging of a single atom, Nat. Photonics **10**, 606 (2016).

[4] U. Wiedemann, K. Karapetyan, C. Dan, D. Pritzkau, W. Alt, S. Irsen, and D. Meschede, Measurement of submicrometre diameters of tapered optical fibres using harmonic generation, Opt. Express **18**, 7693 (2010).

[5] M. Sumetsky and J. M. Fini, Surface nanoscale axial photonics, Opt. Express **19**, 26470 (2011).

[6] J. E. Hoffman, F. K. Fatemi, G. Beadie, S. L. Rolston, and L. A. Orozco, Rayleigh scattering in an optical nanofiber as a probe of higher-order mode propagation, Optica **2**, 416 (2015).

[7] Y. Semenova, V. Kavungal, Q. Wu, and G. Farrell, Submicron accuracy fiber taper profiling using whispering gallery modes in a cylindrical fiber micro-resonator, Proc. SPIE **9634**, 9634 (2015).

[8] J. Keloth, M. Sadgrove, R. Yalla, and K. Hakuta, Diameter measurement of optical nanofibers using a composite photonic crystal cavity, Opt. Lett. **40**, 4122 (2015).

[9] L. S. Madsen, C. Baker, H. Rubinsztein-Dunlop, and W. P. Bowen, Nondestructive profilometry of optical nanofibers, Nano Lett. **16**, 7333 (2016).

[10] T. A. Birks, J. C. Knight, and T. E. Dimmick, High-resolution measurement of the fiber diameter variations using whispering gallery modes and no optical alignment, IEEE Photon. Technol. Lett. **12**, 182 (2000).

[11] M. Sumetsky and Y. Dulashko, Radius variation of optical fibers with angstrom accuracy, Opt. Lett. **35**, 4006 (2010).

[12] S. Holleis, T. Hoinkes, C. Wuttke, P. Schneeweiss, and A. Rauschenbeutel, Experimental stress–strain analysis of tapered silica optical fibers with nanofiber waist, Appl. Phys. Lett. **104**, 163109 (2014).

[13] M. van der Mark and L. Bosselaar, Noncontact calibration of optical fiber cladding diameter using exact scattering theory, J. Lightwave Technol. **12**, 1 (1994).

[14] F. Warken and H. Giessen, Fast profile measurement of micrometer-sized tapered fibers with better than 50-nm accuracy, Opt. Lett. **29**, 1727 (2004).

[15] T. F. Krauss, Why do we need slow light? Nat. Photonics **2**, 448 (2008).

[16] Z. Shi, R. W. Boyd, D. J. Gauthier, and C. C. Dudley, Enhancing the spectral sensitivity of interferometers using slow-light media, Opt. Lett. **32**, 915 (2007).

[17] K. Qin, S. Hu, S. T. Retterer, I. I. Kravchenko, and S. M. Weiss, Slow light mach–zehnder interferometer as label-free biosensor with scalable sensitivity, Opt. Lett. **41**, 753 (2016).

[18] C. Kraeh, J. Martinez-Hurtado, A. Popescu, H. Hedler, and J. J. Finley, Slow light enhanced gas sensing in photonic crystals, Opt. Mater. **76**, 106 (2018).

[19] S. Ek, P. Lunnemann, Y. Chen, E. Semenova, K. Yvind, and J. Mork, Slow-light-enhanced gain in active photonic crystal waveguides, Nat. Commun. **5**, 5039 (2014).

[20] J. F. McMillan, X. Yang, N. C. Panoiu, R. M. Osgood, and C. W. Wong, Enhanced stimulated raman scattering in slow-light photonic crystal waveguides, Opt. Lett. **31**, 1235 (2006).

[21] K. McGarvey-Lechable and P. Bianucci, Maximizing slow-light enhancement in one-dimensional photonic crystal ring resonators, Opt. Express **22**, 26032 (2014).

[22] S. Yan, X. Zhu, L. H. Frandsen, S. Xiao, N. A. Mortensen, J. Dong, and Y. Ding, Slow-light-enhanced energy efficiency for graphene microheaters on silicon photonic crystal waveguides, Nat. Commun. **8**, 14411 (2017).

[23] B. Corcoran, C. Monat, C. Grillet, D. J. Moss, B. J. Eggleton, T. P. White, L. O'Faolain, and T. F. Krauss, Green light emission in silicon through slow-light enhanced third-harmonic generation in photonic-crystal waveguides, Nat. Photonics **3**, 206 (2009).

[24] C. Xiong, C. Monat, A. S. Clark, C. Grillet, G. D. Marshall, M. J. Steel, J. Li, L. O'Faolain, T. F. Krauss, J. G. Rarity, and B. J. Eggleton, Slow-light enhanced correlated photon pair generation in a silicon photonic crystal waveguide, Opt. Lett. **36**, 3413 (2011).

[25] M. Sumetsky, Delay of Light in an Optical Bottle Resonator with Nanoscale Radius Variation: Dispersionless, Broadband, and low Loss, Phys. Rev. Lett. **111**, 163901 (2013).

[26] Optical resonators with whispering-gallery modes-part I: Basics, IEEE J. Sel. Top. Quantum Electron. **12**, 3 (2006).

[27] See Supplemental Material at http://link.aps.org/supplemental/10.1103/PhysRevApplied.14.064052 for additional information, including citation of Refs. [30–34].

[28] M. Tomes, K. J. Vahala, and T. Carmon, Direct imaging of tunneling from a potential well, Opt. Express **17**, 19160 (2009).

[29] M. Foreman, J. Swaim, and F. Vollmer, Whispering gallery mode sensors, Adv. Opt. Photonics **7**, 168 (2015).

[30] A. Oraevsky, Whispering-gallery waves, Quantum Elec. **32**, 377 (2002).

[31] C. C. Lam, P. T. Leung, and K. Young, Explicit asymptotic formulas for the positions, widths, and strengths of resonances in Mie scattering, J. Opt. Soc. Am. B **9**, 1585 (1992).

[32] M. Abramowitz, I. A. Stegun, and D. Miller, *Handbook of Mathematical Functions* (Dover Publications, Washington, DC, 1964), 10th ed.

[33] I. H. Malitson, Interspecimen comparison of the refractive index of fused silica, J. Opt. Soc. Am. **55**, 1205 (1965).

[34] J. R. Buck and H. J. Kimble, Optimal sizes of dielectric microspheres for cavity QED with strong coupling, Phys. Rev. A **67**, 033806 (2003).